

On the Complex Intermetallics in an Al-Mn-Sc Based Alloy Produced by Laser Powder Bed Fusion

Dina Bayoumy^{1,2}, Torben Boll³, Daniel Schliephake⁴, Xinhua Wu^{1,2}, Yuman Zhu^{1,2,*}, Aijun Huang^{1,2,*}

¹ Monash Centre for Additive Manufacturing, 15-17 Normanby Rd, Notting Hill, VIC 3168, Australia

² Department of Materials Science and Engineering, Monash University, Clayton, VIC 3800, Australia

³ Karlsruhe Nano Micro Facility (KNMF), Karlsruhe Institute of Technology (KIT), Hermann-von-Helmholtz-Platz 1, D-76344, Eggenstein-Leopoldshafen, Germany

⁴ Institute for Applied Materials (IAM-WK), Karlsruhe Institute of Technology (KIT), Engelbert-Arnold-Straße 4, D-76131 Karlsruhe, Germany

Abstract

The recently-developed Al-Mn-Sc based alloys specific for laser powder bed fusion (LPBF) have shown excellent mechanical performance. However, the complicated intermetallic particles in the microstructure remain to be identified, hindering the deep understanding of their effects on mechanical properties and further property improvement. In this work, a range of phases in a LPBF-built Al-Mn-Sc based alloy have been systematically studied by atom probe tomography. The results clarify characteristic intermetallic phases in two different grain-size regions in the microstructure. In the fine grain (FG) region, three distinct phases have been identified. A Sc-rich phase having an average composition of $\text{Al}_{3.3}(\text{Sc}_{0.8}\text{Zr}_{0.2})$ is observed at both the grain boundary (GB) and grain interior, but they have different morphologies. The Mn-rich phase with an average composition of $\text{Al}_{4.3}(\text{Mn}_{0.9}\text{Fe}_{0.1})$ is only observed along GBs. In addition, Mg-rich oxide has been observed either with a separate distribution or attached to Sc-rich particles. In the coarse grain (CG) region, the GB particles exhibit different size and composition from FG region. The Sc-rich GB particles contain Mg enrichment rather than Zr and the composition is determined to be $\text{Al}_{3.4}(\text{Sc}_{0.75}\text{Mg}_{0.25})$. The Mn-rich GB particles in the CG region, with higher Fe contents, are $\text{Al}_{4.3}(\text{Mn}_{0.8}\text{Fe}_{0.2})$ along the GBs and $\text{Al}_{4.5}(\text{Mn}_{0.85}\text{Fe}_{0.15})$ inside the grains. Many smaller Mg-rich oxides and Sc-rich particles are also observed in the internal grains of the CG region.

Keywords: Al alloys; Laser powder bed fusion; Intermetallics; Composition; Atom probe tomography

* Corresponding authors.

E-mail addresses: yuman.zhu@monash.edu (Y.M. Zhu), aijun.huang@monash.edu (A.J. Huang)

1. Introduction

Laser powder bed fusion (LPBF) is one of the major additive manufacturing (AM) techniques that has attracted growing attention due to its high capability to rapidly manufacture metallic parts with high geometrical complexity [1,2]. Therefore, it has been explored to produce various Al alloys with a high strength to weight ratio to be used in the transportation and aerospace industries [3]. Among these LPBF Al alloys, it was found that the addition of Sc can effectively overcome the hot tearing issue associated with the AM process while significantly improving the alloy strength. Thus, a number of Sc-containing Al alloys have been recently developed that are specifically for the LPBF process [4]. Typically, a commercial alloy named Scalmalloy, which is a Sc-modified Al-Mg based alloy, has been reported to have a yield strength (YS) of 290 MPa with an elongation exceeding 15% [5]. Recently, a Sc-modified Al-Mn alloy has also been developed for LPBF that has even better mechanical properties [6], where a YS of 430 MPa with an elongation exceeding 17% was achieved by LPBF [7].

The excellent mechanical properties of these Sc-containing LPBF Al alloys were attributed to their unique microstructures that are apparently different from those by conventional fabrication methods. The common microstructural features of the Sc-containing Al alloys fabricated by LPBF involve a bimodal grain structure, i.e., equiaxed fine-grains at the bottom of the melt pools and columnar coarse-grains in the remainder of the melt pools [5,7–10]. Further, in these bimodal grains, a range of intermetallic particles have been observed in different Sc-containing Al alloy systems [7,9–11]. Many of these intermetallic particles are distributed along the grain boundaries. Thus, they were suggested to play an important role in pinning grain boundaries, resisting the grain growth during LPBF processing and thus significantly influencing the mechanical properties of these alloys [11]. Given the importance of these intermetallic particles, efforts have been previously undertaken to identify their distribution, crystal structure, and composition [7,11–14]. So far, these intermetallic phases from the LPBF process can be generally summarized into three types depending on the alloy systems: Al-Sc phase, Al-Mn phase and oxides.

The Al-Sc phase was initially reported to be in the form of Al_3Sc with the L_{12} structure (face-centered cubic, $a = 0.41$ nm) [15]. The Al_3Sc particles were suggested to form at high temperatures (up to 800°C) from the melt during the LPBF process [11], which makes it an effective heterogeneous nucleation site for the subsequent solidification and formation of α -Al grains [16]. Later on, it was reported that the Sc in Al_3Sc could be partially replaced by transition metal (TM) elements in some ternary or quaternary Sc-containing alloy systems and thus, the composition can be expressed by $\text{Al}_3(\text{Sc}_{1-y}\text{X}_y)$, where X represents TM elements [17]. Moreover, it has been stated that the grain refinement effect of Al_3Sc can be enhanced by the addition of TM elements such as Zr, which substitutes some Sc atoms and further reduces the lattice mismatch with Al [18]. In addition, the $\text{Al}_3(\text{Sc}_{1-y}\text{Zr}_y)$ -type particles normally exhibit a core-shell structure that has higher thermal stability [16,19–23]. Aside from the formation of $\text{Al}_3(\text{Sc}_{1-y}\text{Zr}_y)$ particles, Al-Mg oxides have also been identified in the microstructure of Scalmalloy in the form of MgAl_2O_4 (spinel), Al_2O_3 or MgO particles. While the formation of these oxides possibly originates from the thin oxide layer coating the Al powder particles, they have been suggested to play a supportive role, along with Al_3Sc or $\text{Al}_3(\text{Sc}_{1-y}\text{X}_y)$, in refining the microstructure [11]. As for the Al-Mn phase, a recent atom probe tomography study [10] has confirmed that ~4.3 wt.% of Mn can be retained in supersaturated solid solution in the Al matrix in an Al-2.29Mn-1.51Mg-0.49Sc-0.23Zr (at.%) alloy, owing to the rapid cooling from LPBF (the equilibrium limit of Mn solubility in Al is ~1.6 wt.% [24]). Yet, a number of Mn-rich particles form preferentially at grain or subgrain boundaries. These particles had a

quasicrystalline structure with a chemical composition of ~86 at.% Al and ~13 at.% Mn [12]. Such stoichiometry has been correlated to the Al₆Mn phase. Other metastable structures that consist of either icosahedral or decagonal quasicrystal phases can potentially form in rapidly solidified Al-Mn alloys [24–26]. In addition, it has been indicated that the formation of Al-Mn particles from solid solution can be accelerated by the presence of Fe [27]. In other words, the element Fe can replace some Mn atoms in the Al-Mn particles. In this situation, the Al-Mn particles were expressed by Al₆(Mn, Fe) [27,28], for which a quasicrystal with a 10-fold symmetry has been identified in an Al-Mn-Sc alloy produced by LPBF [7].

From the above previous work, the phases formed in many Sc-containing Al alloys are quite complex. Their chemistry, morphology and distribution are often dissimilar in different alloy systems. Due to their significant effects on the mechanical properties [8,10,29–31], the full understanding of their chemistry and distribution in a certain alloy system is thus critical for any further property improvement. This is particularly important given that the conventional homogenization step was not able to dissolve the intermetallic particles formed in the supersaturated Al-Mn-Sc based alloys produced by LPBF. Consequently, this study aims to provide a systematic investigation on the types and chemistry of various secondary phases that form in an Al-Mn-Sc based alloy produced by LPBF. Our previous work has reported that this alloy has excellent mechanical performance [7,10]. However, the phases formed from the LPBF process remain to be clearly established due to their complexity. This work is accomplished by extensive use of atom probe tomography (APT) analysis to reveal the accurate compositions of the different phases existing in the different microstructural regions in the as-fabricated (AF) condition.

2. Methods

2.1. Specimen preparation

The powder used in this study was gas atomized from cast ingots through a vacuum induction gas atomization (VIGA) process. The chemical composition of the powders was Al-2.32Mn-1.42Mg-0.56Sc-0.13Zr-0.03Fe-0.04Si (at.%), i.e., Al-4.58Mn-1.24Mg-0.91Sc-0.42Zr-0.07Fe-0.04Si (wt.%), as measured by inductively coupled plasma atomic emission spectroscopy (ICP-AES). The alloy powders are within the size range of 20–70 μm with an average value of around 35 μm. The average values of the cumulative powder diameter at 10% (D₁₀), 50% (D₅₀), and 90% (D₉₀) of the powder volume are of 23.6 μm, 34.9 μm and 51.6 μm, respectively. The powders were processed by a commercial EOS M290 powder-bed machine equipped with a Yb-fiber laser with a wavelength of 1070 nm, maximum power of 400 W and a spot size of around 100 μm in diameter. The LPBF processing was performed under a controlled Argon environment with a minimum oxygen level of 0.1 vol. %. Based on the process parameter optimization study, samples were built using 350 W (laser power), 1600 mm/s (scan speed), 0.1 mm (hatch distance) and 30 μm (layer thickness) with a laser beam rotation of 67° alternating between consecutive layers.

2.2. Microstructure characterization

Samples for scanning electron microscopy (SEM) imaging were cut from the built samples, ground to 2400 Grit size, and polished using silica colloidal suspension. The backscattered electron (BSE) imaging was performed on a JEOL 7001F field emission gun (FEG) SEM.

The tip-shaped samples for the APT were prepared by the lift-out technique across equiaxed fine-grains (FG) and columnar coarse-grains (CG) regions of the AF samples using site-

specific preparation of focused ion beam (FIB) on a Zeiss Auriga Dual Beam FIB using Ga⁺ ions. To reduce the damage caused by the Ga⁺ ion beam, the region of interest was protected by a layer of Pt before milling, as described by Larson *et al.* [32]. All lift-outs were milled perpendicular to the LPBF build direction, as illustrated in Fig. 1. Atom probe acquisition was carried out in a Local Electrode Atom Probe (LEAP) Cameca 4000 XHR under an ultra-high vacuum and a set temperature of 50 K. The standing high voltage was controlled by the detection rate set to 0.5%. The device was operated using laser pulsing with a pulse energy of 30 pJ and a 100-200 kHz pulse repetition rate. The APT data were reconstructed and analyzed using Cameca IVAS 3.6.14 software. The isoconcentration surfaces employed a concentration of 5 at.% (Mg + Sc + Zr + Fe + O) and 10 at.% (Mn). The composition of phases was determined using the proximity histogram method [33].

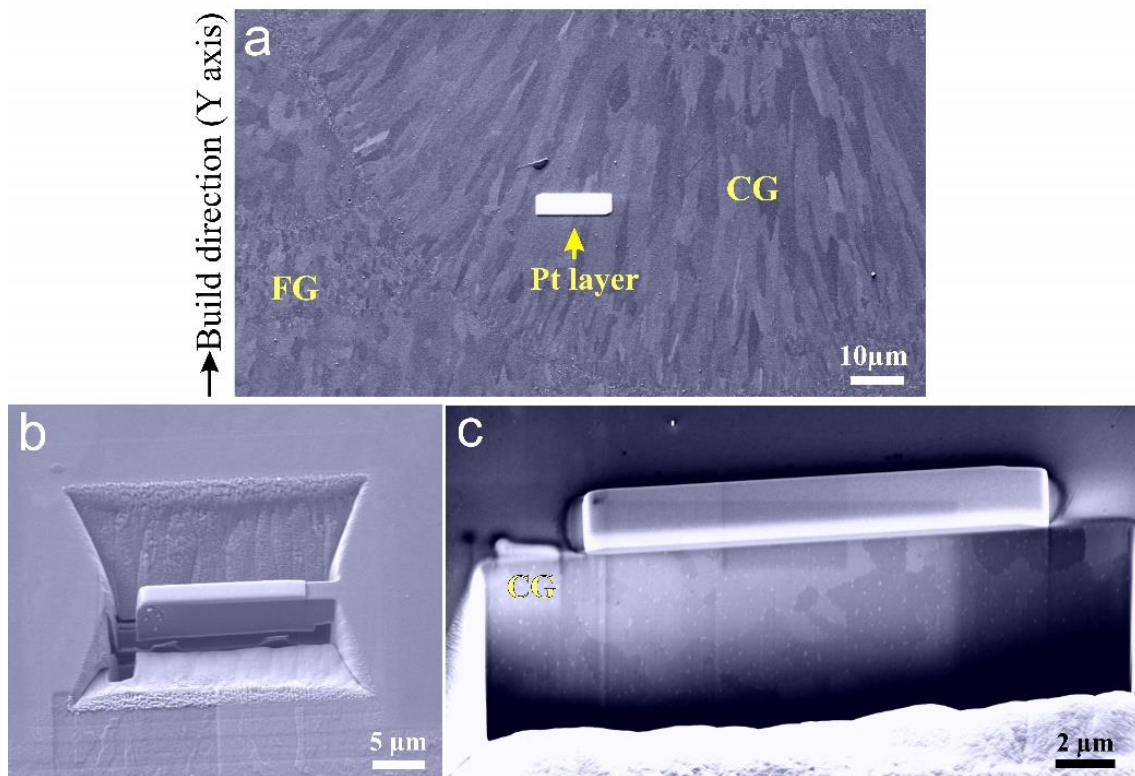


Fig. 1. (a) SEM-BSE image of the microstructure along the LPBF build direction showing a Pt layer covering part of a CG region, (b) SEM image showing a slice in a CG region milled by FIB, and (c) SEM-BSE image revealing the microstructure of a CG lift out.

3. Results and discussion

Fig. 2(a) shows the typical bimodal grain structure in the LPBF-fabricated alloy. A section perpendicular to the building direction reveals the alternating distribution of CG and FG regions. In addition, many bright particles are observed inside these grains and along their grain boundaries, as shown in Fig. 2(b-d). The contrast between the particles and the matrix originates from the sensitivity of BSE imaging to the higher atomic number of these particles compared to Al. A comprehensive explanation of the bimodal microstructure of this alloy has been provided in our recent work [7,30]. Here, the intragranular particles in the matrix region are designated IGP, whereas the grain boundary (GB) particles are termed GBP for simplicity.

Close examination of Fig. 2(b) and 2(d) indicates that the density of GBPs in the FG region is higher than that in the CG region.

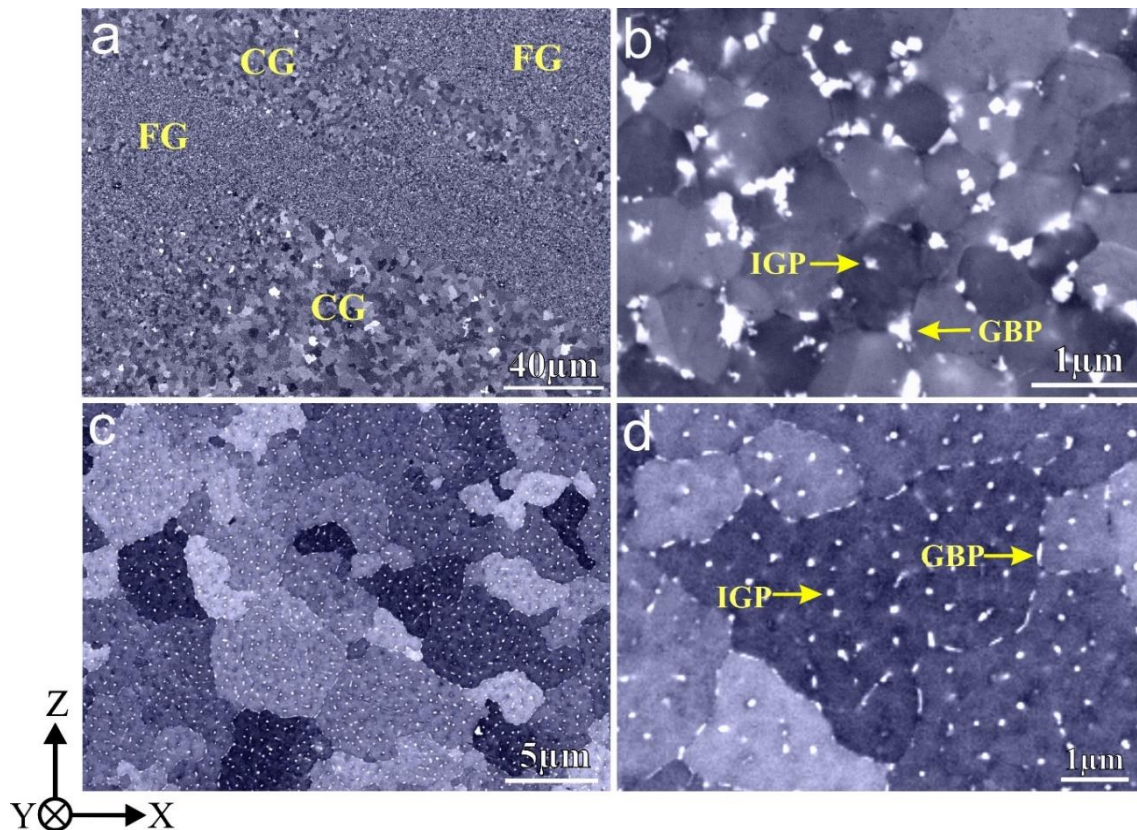


Fig. 2. (a) SEM-BSE image revealing a bimodal microstructure of FG regions interspersed with CG regions in an AF sample cut perpendicular to the build direction, (b) enlarged image from an FG region in (a) showing many intermetallic particles existing inside the matrix and along grain boundaries, (c-d) enlarged images from a CG region in (a) showing intermetallic particles inside the matrix and along grain boundaries. The particles in CG and FG along grain boundaries and inside grains are designated GBP and an IGP, respectively.

3.1. Intermetallic Phases in FG region

All the particles existing in the FG region were studied by APT to reveal their chemistry. Fig. 3 provides APT reconstruction maps showing the element distribution in a tip-sample containing a grain boundary segment. Inspection of these elemental maps reveals a high concentration of solute elements at the GB region (GBP) and a bottom region inside the grains (IGP). In the remaining regions, solute elements are uniformly distributed without clustering or interaction between Mn, Mg, Sc, and Zr.

The GBPs in Fig. 3 were further displayed with isoconcentration surfaces in Fig. 4(a-b). Two irregularly-shaped particles contacting each other are enriched in Mn and Sc, respectively. The proximity histogram in Fig. 4(c) displays the composition profile across the interface between the α -Al matrix and the Sc-rich GBP. Every point in the profile represents the atomic concentration of an element relative to all other elements. The analysis reveals that the Sc-rich GBP particle comprises around 76 at.% Al, 18.5 at.% Sc and 4.5 at.% Zr, Table 1. According to this composition, the Al concentration is slightly higher than that in the equilibrium Al_3Sc

phase, while the relatively low concentration of Sc is compensated mainly by Zr although minor other elements are also presented. Therefore, such Sc-rich GBP particles can be approximately expressed by $\text{Al}_{3.3}(\text{Sc}_{0.8}\text{Zr}_{0.2})$. It is interesting to find that the Zr element in this GBP is mainly distributed in the core part of the particle, Fig. 4(b).

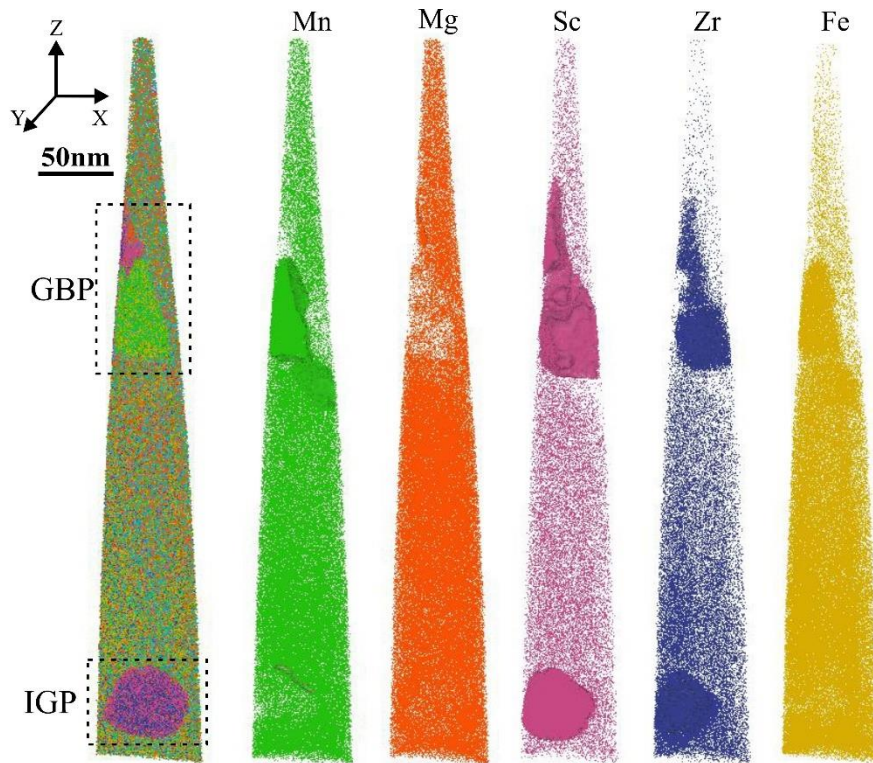


Fig. 3 APT reconstruction elemental maps of a tip-sample from FG region containing a grain boundary segment.

As for the Mn-rich GBP, a minor Fe concentration can be identified apart from the Mn. According to the composition profile in Fig. 4(d), the average composition of the Mn-rich GBP contains 81 at.% Al, 17 at.% Mn, and 1.9 at.% of Fe, Table 1. Thus, the composition of the Mn-rich GBP can be roughly expressed as $\text{Al}_{4.3}(\text{Mn}_{0.9}\text{Fe}_{0.1})$. This phase has been previously identified to have a ten-fold quasicrystal structure [7]. It should be noted that the element Fe normally exists as an inevitable impurity in commercial-purity Al alloys. Moreover, Fe has been suggested to replace some Mn atoms to form the $\text{Al}_6(\text{Mn}, \text{Fe})$ phase [27,35]. However, the composition shown here for the Mn-rich GBP is different from these previous reports [27,35]. The reason behind the formation of this phase rather than the equilibrium $\text{Al}_6(\text{Mn}, \text{Fe})$ in LPBF might be the quenching effect caused by ultrafast cooling rates $\sim 10^6$ K/s [11,25,26]. In addition, Fe can play a role in stabilizing the quasicrystal phase [36,37].

Apart from the $\text{Al}_{3.3}(\text{Sc}_{0.8}\text{Zr}_{0.2})$ and $\text{Al}_{4.3}(\text{Mn}_{0.9}\text{Fe}_{0.1})$ GBP particles identified from Fig. 4, some Mg-rich particles (<20 nm) are also present, as shown by the orange surfaces in Fig. 4(a-b). Typically, strong segregation of Mg atoms to GBs has been previously identified [38,39]. This segregation may provide a barrier against GB migration and improve microstructural stability [40].

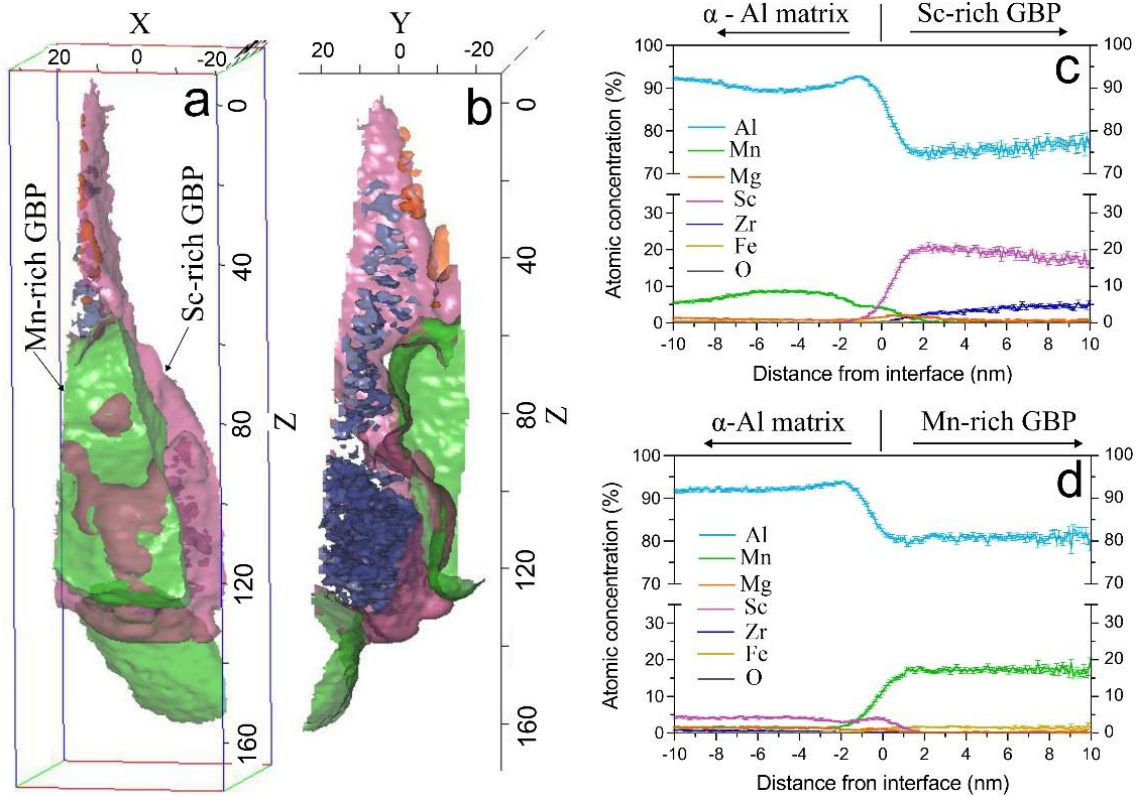


Fig. 4. (a-b) GBPs highlighted with isoconcentration surfaces and (c-d) corresponding proximity histograms showing the composition profile of Sc-rich GBP and Mn-GBP respectively.

The Sc-rich IGP detected in the grain interior of FG region in Fig. 3 has a size of ~40–50 nm. The particle exhibited a nearly-cubic morphology but with some facets, as shown in Fig. 5(a-b). In addition, very fine perturbations can be seen on the surface. Again, an obvious Zr enrichment in the particle core can be clearly identified. The similar distribution has also been observed previously in the direct energy deposited Al-Sc-Zr alloys [34]. Yet, this distribution in the Sc-rich GBP is the inverse of the secondary $\text{Al}_3(\text{Sc}, \text{Zr})$ particles from solid-state precipitation during post heat treatments, for which the Sc-rich core and Zr-rich shell structure was usually observed [22,23]. It seems the entrapment of Zr within these Sc-rich IGP particles can influence the amount of supersaturated Zr in the matrix [34]. If this is a case that there is no sufficient Zr left in the matrix to diffuse to the secondary $\text{Al}_3(\text{Sc}, \text{Zr})$ precipitates during post heat treatments, then the Zr bound observed in Sc-rich IGP and GBP might be the reason for the absence of the similar core-shell structure in the secondary precipitates [10,30,34].

The APT analysis reveals a quite similar average composition to the $\text{Al}_{3.3}(\text{Sc}_{0.8}\text{Zr}_{0.2})$ GBP. The cubic morphology seems to imply that these particles form in the melt prior to the solidification of $\alpha\text{-Al}$ [15,41]. They have been suggested to be effective nuclei for the later solidification of refined $\alpha\text{-Al}$ grains [16]. It should be emphasized that these faceted cubic particles were only observed in the FG region, which is consistent with our previous report [7]. This phenomenon implies that the remarkable refinement of FG compared to CG, Fig 2(a), is caused by the abundance of these seed crystals in FG. Considering the hypereutectic composition of our alloy (0.91 wt.%), which is beyond the eutectic composition (~0.6 wt. % [16]), many primary Sc-rich IGP or Sc-rich GBP particles are expected to form during solidification. It was also suggested that the excess particles, that did not act as nuclei for grain solidification as Sc-rich

IGP, were pushed by the solidification front of α -Al towards the grain boundary, which leads to the formation of the Sc-rich GBP [41]. Such Sc-rich GBP plays a role in controlling the size of the GB [42] at different levels of laser energy input [7]. Afterward, these Sc-rich GBP could further grow due to the cyclic reheating during the layer-by-layer fusion or during the deposition of adjacent tracks. The growth of the Sc-rich GBP (~ 140 nm, Fig. 4) compared to Sc-rich IGP (~ 50 nm, Fig. 5) might be accelerated by the enhanced solute diffusion along the GB regions [43]. There is also a possibility that some of the Sc-GBPs may have formed in the solute-enriched GB.

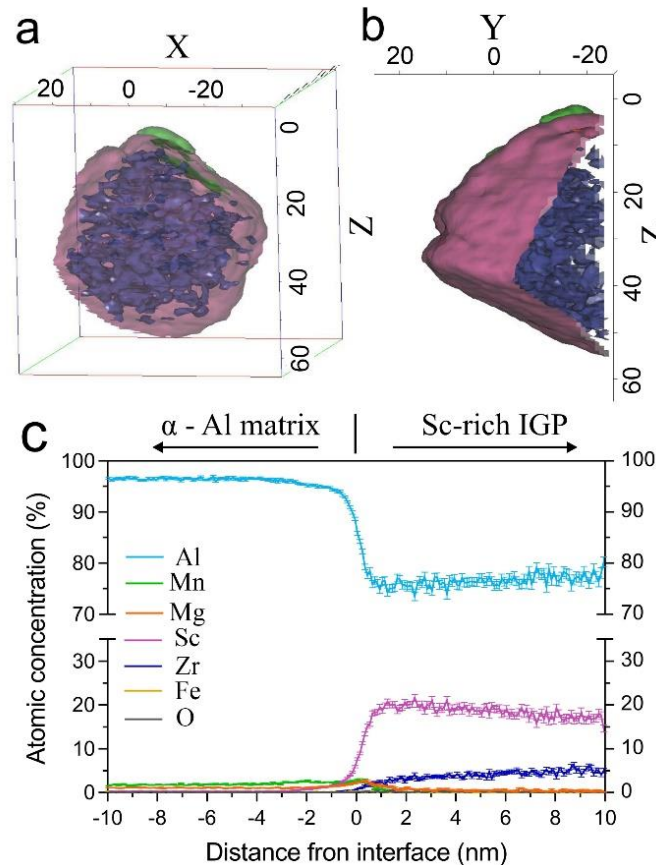


Fig. 5 (a-b) IGP observed in Fig. 3 highlighted with isoconcentration surfaces, and (c) corresponding proximity histogram showing the composition profile of IGP.

Another IGP particle with a composition close to $\text{Al}_{3.3}(\text{Sc}_{0.8}\text{Zr}_{0.2})$ was captured in a different area of FG next to a Mg-rich IGP particle, Fig. 6. The presence of oxygen in this IGP has been confirmed by the proximity histogram analysis in Fig. 6(c) along with Al and Mg, which confirm that this is a Mg-rich oxide inclusion. A similar Al-Mg oxide/Sc-IGP couple has been reported in the microstructure of a Mg-rich Al alloy, such as Scalmalloy [11]. However, it should be noted that the Al content in such an inclusion might be overestimated due to the local magnification effect, which may be pronounced here due to the small size of the particle [44]. In previous work, it has been suggested that oxide inclusions might act as grain refiners [45] or as heterogeneous nucleation sites for the following formation of primary Sc-rich IGP precipitation since they precipitate in the melt prior to Al_3Sc [11,46]. Therefore, it is probable that the Sc-rich IGPs tend to nucleate around some of these oxide particles. Yet, a similar oxide inclusion has not been observed next to the Sc-rich IGP in Fig. 5. This seems to imply that the heterogeneous nucleation of Sc-rich IGP on the surface of oxides is not necessarily the

dominant nucleation mechanism. In general, the formation of oxides confirms that even in an argon atmosphere with an oxygen level of ~0.1 vol.%, oxidation may not be completely suppressed during the LPBF processing of Al.

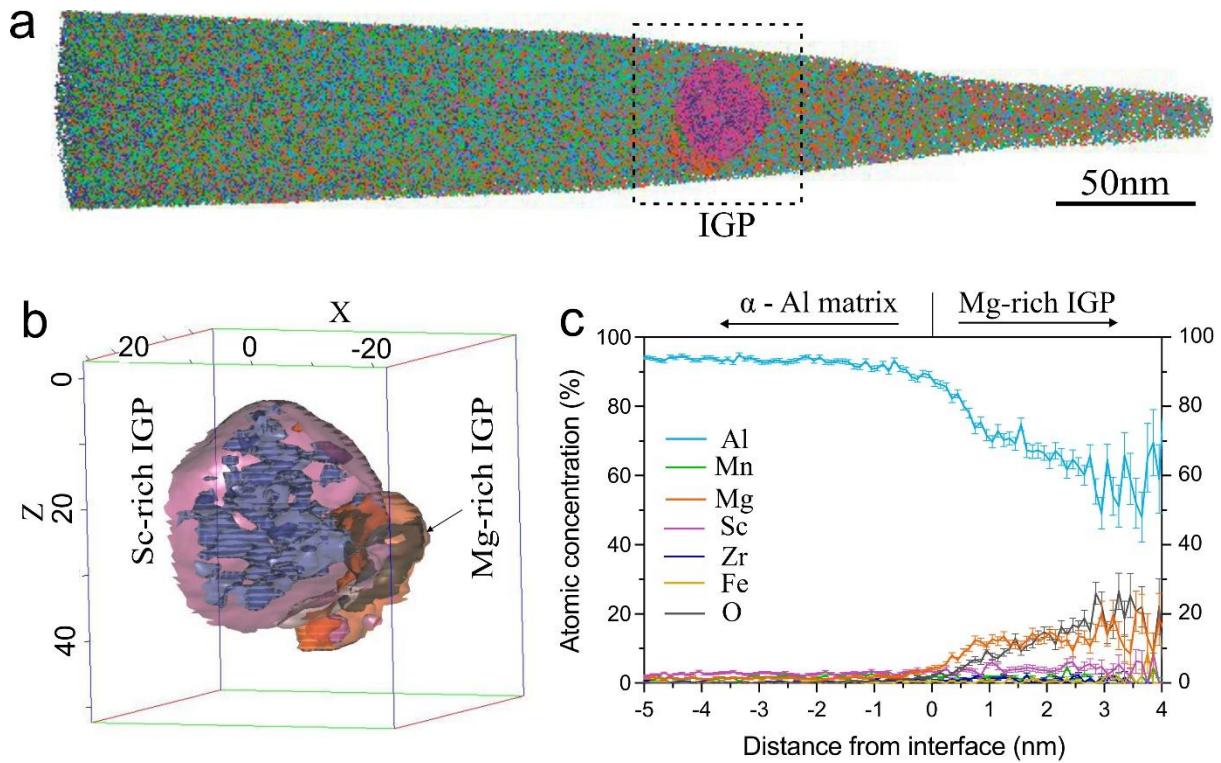


Fig. 6 APT reconstruction showing (a) atom map of a tip in FG region incorporating an IGP, (b) the IGP observed in (a) highlighted with isoconcentration surfaces (dimension in nm), (c) proximity histogram showing the composition profile of the Mg-IGP attached to Sc-IGP.

Table 1 Average composition (at.%) of the particles observed in FG and CG in the AF condition.

Particles in AF microstructure	Atomic percentage of elements (at.%)							
	Al	Mn	Mg	Sc	Zr	Fe	O	
FG	Sc-rich GBP	76.0 ± 1.0	0.3 ± 0.1	0.5 ± 0.3	18.5 ± 1.2	4.5 ± 0.7	0.1 ± 0.1	0.1 ± 0.1
	Mn-rich GBP	80.9 ± 0.5	17.0 ± 0.5	0.2 ± 0.1	0.0	0.0	1.9 ± 0.2	0.0
	Sc-rich IGP	76.5 ± 1.1	0.0	0.5 ± 0.2	18.5 ± 1.3	4.3 ± 0.8	0.1 ± 0.1	0.1 ± 0.1
CG	Sc-rich GBP	76.1 ± 1.2	0.7 ± 0.4	5.4 ± 0.9	16.9 ± 1.1	0.4 ± 0.6	0.4 ± 0.4	0.1 ± 0.1
	Mn-rich GBP	80.4 ± 2.9	15.0 ± 2.7	0.3 ± 0.6	0.3 ± 0.4	0.1 ± 0.2	3.5 ± 1.7	0.1 ± 0.3
	Sc-rich IGP	75.1 ± 1.4	0.8 ± 0.4	5.2 ± 0.8	17.2 ± 1.0	0.6 ± 0.4	0.6 ± 0.4	0.5 ± 0.3
	Mn-rich IGP	81.0 ± 0.4	15.3 ± 0.2	0.5 ± 0.2	0.1 ± 0.0	0.1 ± 0.0	2.7 ± 0.2	0.4 ± 0.1

3.2. Intermetallic Phases in CG region

Having identified various intermetallic particles in the FG region, we further examined the particles in the CG region. Fig. 7 shows the APT reconstructed maps from a CG region containing both GBP and IGP. In comparison to the GBPs observed in the FG region in Fig. 3, the GBPs in the CG region seem smaller in size, and this is also consistent with our SEM observations shown in Fig. 2. One possible reason for this phenomenon is the higher volume fraction of grain boundaries in FG than CG, which can be more effective as diffusion channels to stimulate the rapid diffusion of elements to form GBP phases during laser fusion and subsequent cyclic reheating [43].

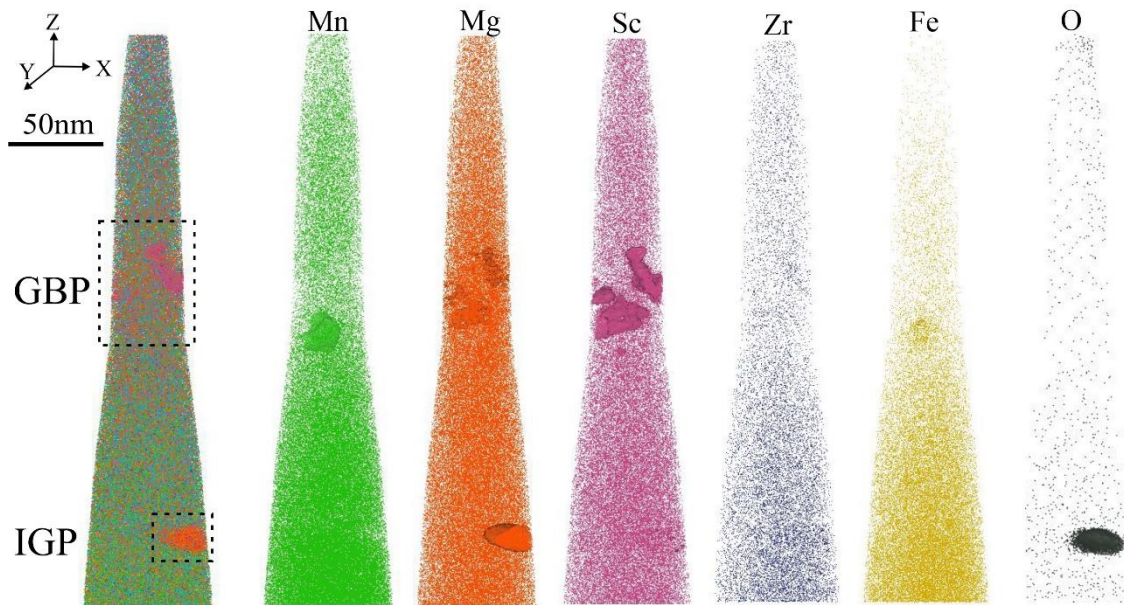


Fig. 7 APT reconstructed elemental maps of a tip from the CG region.

However, the further analysis for the Sc-rich GBP, provided in Fig. 8, reveals a different stoichiometry from that in FG in Fig. 4. The Sc-rich GBP in CG contains almost no Zr (Table 1). Instead, Mg enrichment (~ 5 at.%) is revealed mainly in the particle core, as shown in Fig. 8(b). Also, there are many separate Mg-rich particles (no Sc contents) attached to the Sc-rich particle, as shown by the orange isoconcentration surface in Fig. 8(a). Based on this analysis, the composition of Sc-rich GBP can be expressed by $\text{Al}_{3.4}(\text{Sc}_{0.75}\text{Mg}_{0.25})$, although minor Mn is also present. Apart from the Sc-rich GBP, the Mn-rich GBP has also been observed in the CG region, Fig. 8(c), with a higher Fe concentration (~ 3.5 at.%) than in the FG region. This higher concentration of Fe is compensated by a decrease in the level of Mn, leading to the composition of $\text{Al}_{4.3}(\text{Mn}_{0.8}\text{Fe}_{0.2})$.

Furthermore, another type of Mg-oxide has been observed in the grain interior of CG, as revealed by Fig. 9. The composition analysis based on the concentration profile in Fig. 9(b) revealed a Mg:Al:O ratio of $\sim 1:2.2:2.5$. This suggests that this inclusion might be the spinel (MgAl_2O_4), considering the oxygen concentration is being underestimated in APT due to the evaporation of neutrals [47,48]. Interestingly, this oxide inclusion in Fig. 9(a) shows a Mg layer encircling the oxide inclusion, i.e., oxygen is localized in the core more than the periphery.

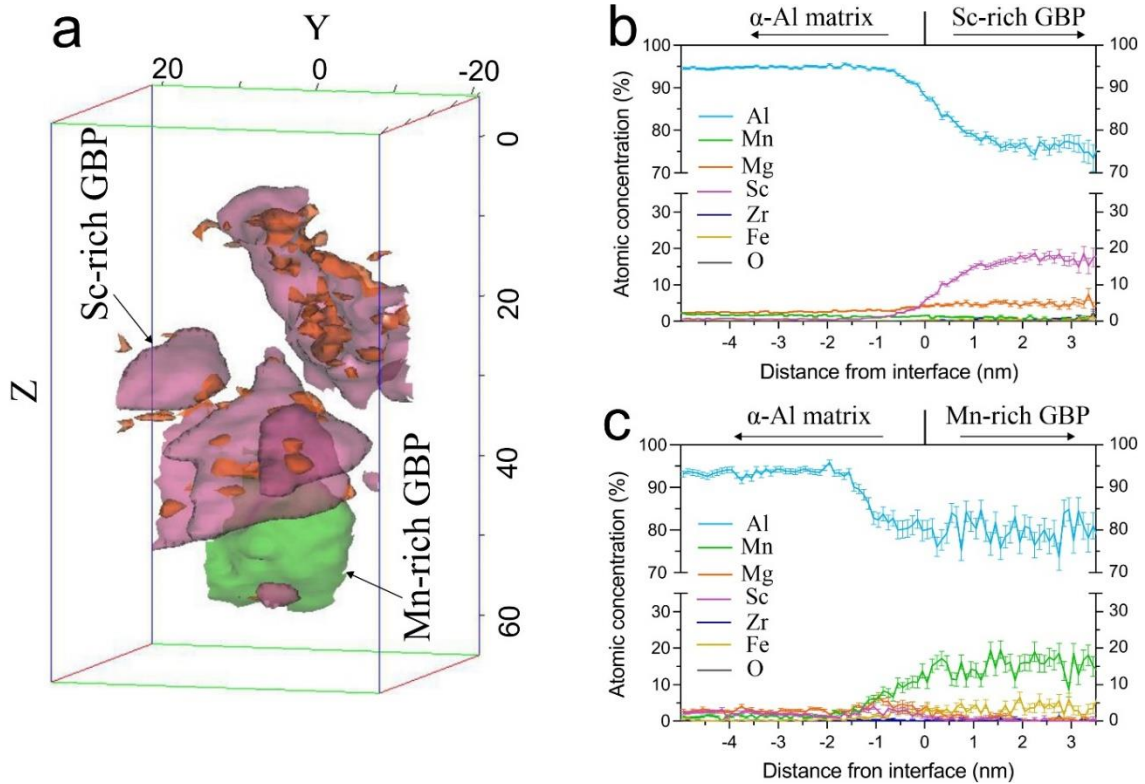


Fig. 8 (a) GBPs in CG highlighted with isoconcentration surfaces, and (b-c) proximity histograms showing the composition profile of (b) Sc-rich GBP and (c) Mn-rich GBP.

Apart from the Mg-rich IGP, we have also observed other complicated IGP in a different CG area, as shown in Fig. 10. Close inspection of the features along the isoconcentration surfaces in Fig. 10(b) reveals that this particle is actually a conglomeration of three different types of particles: Sc-rich IGP, Mn-rich IGP, and Mg-rich IGP. The proximity histogram in Fig. 10(c) reveals small and scattered Sc-rich IGP. Still, they have a similar composition to the Sc-rich GBP observed in the CG region (table 1). For the Mn-rich IGP, its composition based on Fig. 10(d) can be expressed by $\text{Al}_{4.5}(\text{Mn}_{0.85}\text{Fe}_{0.15})$. It has been suggested that the Mn-rich IGP, observed exclusively in the CG region, might form by solute segregation along intracrystalline dislocation walls constituting subgrain boundaries [10,12].

As for the Mg-rich IGP, which is clearly an oxide inclusion, it has relatively higher oxygen contents than the Mg-rich IGP inclusion in Fig. 9. However, similar to the above observed Mg-rich IGP, this oxide also reveals an oxygen enrichment towards the particle's core. The oxygen enrichment in these Mg-rich inclusions is expected to be derived from the tenacious oxide layer covering the Al powder [49]. Furthermore, tiny individual Mg particles are observed at the interface of the IGP particle with the matrix, Fig. 10(e).

From the above observations, Mg oxides appear at GB and intragranular areas in both FG and CG regions. Though these Mg oxides are undesired, they still form driven by the affinity of Mg to oxygen. Typically, Mg oxides form during solidification at a temperature higher than 700 °C [11]. Afterward, these oxides get entrapped in the melt as inclusions. Once such oxide inclusions form, they are difficult to be remelted during processing. They might play an occasional role as grain refiners [45] or contribute to the nucleation of refiners [46]. However, care must be taken that these oxides which are harder than the matrix do not act as notches

affecting the strength and fatigue life [50]. Therefore, the Mg amount in the alloy composition of this work has been limited to below 1.5 at.% to control the amount of these Mg oxides.

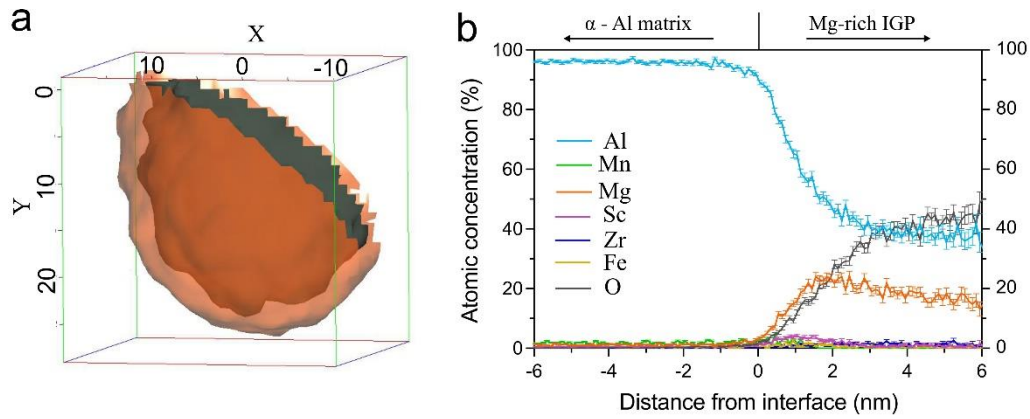


Fig. 9 (a) IGP observed in Fig. 7 highlighted with isoconcentration surface, and (b) corresponding proximity histogram showing the composition profile of this Mg-rich IGP particle.

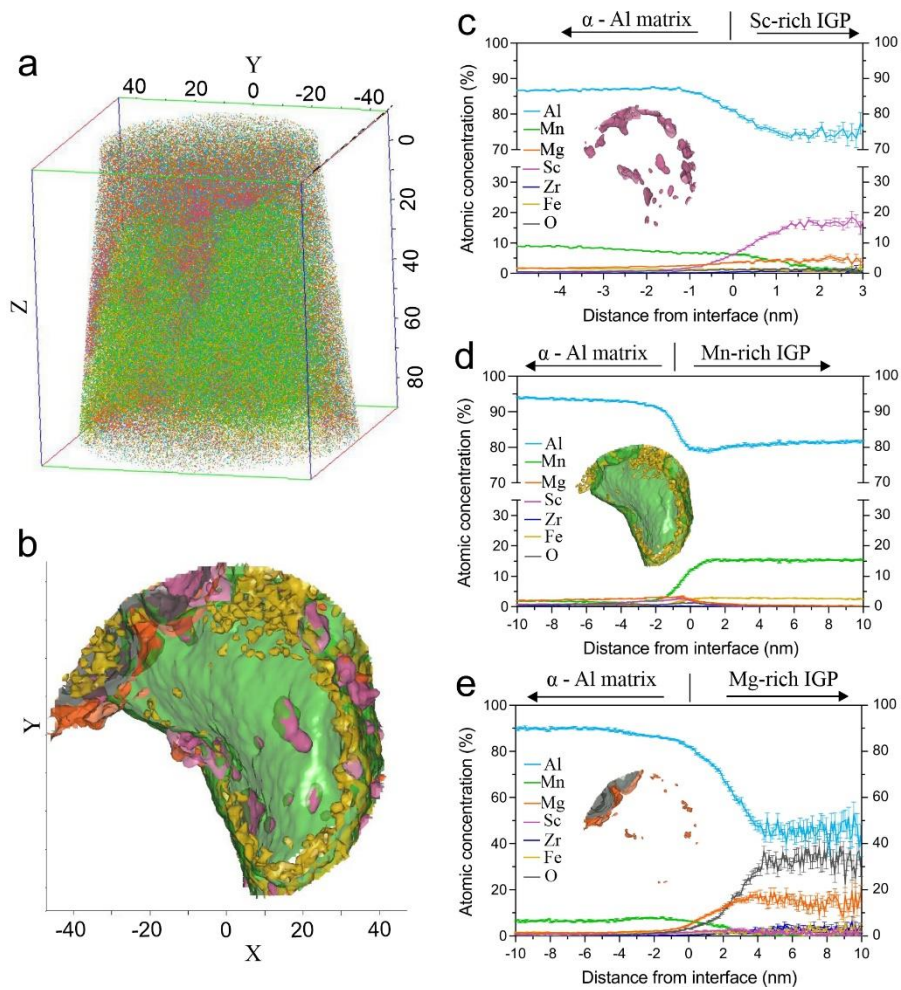


Fig. 10 (a) 3D atom maps in CG revealing IGP, (b) IGP highlighted with isoconcentration surfaces (dimension in nm), proximity histograms showing the composition profile of (c) Sc-rich IGP, (d) Mn-rich IGP and (e) Mg-rich IGP.

4. Conclusions

In this work, the chemical compositions of various phases exhibited in the microstructure of Al-Mn-Sc alloys produced by LPBF have been systematically studied and identified by atom probe tomography. The main conclusions can be summarized as follows:

1. There are three totally different types of phases that have been identified in the FG region of the LPBF-built microstructure. These phases are distributed along grain boundaries (GBPs) and inside grains (IGPs). Two different GBPs enriched in dominant Sc and Mn elements, respectively, are attached to each other. The average composition of Sc-rich GBP is determined to be $\text{Al}_{3.3}(\text{Sc}_{0.8}\text{Zr}_{0.2})$. The Mn-rich GBP has an average chemical composition of $\text{Al}_{4.3}(\text{Mn}_{0.9}\text{Fe}_{0.1})$. Inside the FGs, the Sc-rich IGP particles with similar $\text{Al}_{3.3}(\text{Sc}_{0.8}\text{Zr}_{0.2})$ composition and element distribution are also observed, but with a more regular shape. In addition, Mg-rich oxide IGP has been observed either with separate distribution or attached to Sc-rich IGP.
2. In the CG region of the LPBF-built microstructure, two distinct GBPs have also been identified. These GBPs exhibit smaller sizes than those in the FG region. In addition, their compositions are also different from FG region. The Sc-rich GBP contains Mg enrichment rather than Zr and the composition is determined to be $\text{Al}_{3.4}(\text{Sc}_{0.75}\text{Mg}_{0.25})$. For the Mn-rich GBP in the CG region, the Fe content is higher than that in the FG, leading to a different composition formula of $\text{Al}_{4.3}(\text{Mn}_{0.8}\text{Fe}_{0.2})$. As for the IGPs, different from the FG region, the Mn-rich IGPs are also observed. It has a slightly different composition of $\text{Al}_{4.5}(\text{Mn}_{0.85}\text{Fe}_{0.15})$ and is attached by many small Mg-rich oxides and Sc-rich IGPs. The large and regular-shape Sc-rich IGPs were not observed in the CG region.

Acknowledgements

The authors wish to acknowledge the use of instruments and scientific and technical assistance at the Karlsruhe Nano Micro Facility (KNMF) in Germany and the Monash Centre for Electron Microscopy as a Node of Microscopy Australia. The authors thank Mrs. Delphine Chassaing for the FIB preparation of APT tips.

References

- [1] S. Lathabai, Additive Manufacturing of Aluminium-Based Alloys and Composites, in: R.N. Lumley (Ed.), *Fundam. Alum. Metall. Recent Adv.*, Elsevier, 2018: pp. 47–92. <https://doi.org/10.1016/b978-0-08-102063-0.00002-3>.
- [2] T. DebRoy, H.L. Wei, J.S. Zuback, T. Mukherjee, J.W. Elmer, J.O. Milewski, A.M. Beese, A. Wilson-Heid, A. De, W. Zhang, Additive manufacturing of metallic components – Process, structure and properties, *Prog. Mater. Sci.* 92 (2018) 112–224. <https://doi.org/10.1016/j.pmatsci.2017.10.001>.
- [3] N.T. Aboulkhair, M. Simonelli, L. Parry, I. Ashcroft, C. Tuck, R. Hague, 3D printing of Aluminium alloys: Additive Manufacturing of Aluminium alloys using selective laser melting, *Prog. Mater. Sci.* 106 (2019) 100578. <https://doi.org/10.1016/j.pmatsci.2019.100578>.
- [4] P. Rometsch, Q. Jia, K. V. Yang, X. Wu, Aluminum alloys for selective laser melting – towards improved performance, in: F. Froes, R. Boyer (Eds.), *Addit. Manuf. Aerosp. Ind.*, Elsevier, 2019: pp. 301–325. <https://doi.org/10.1016/b978-0-12-814062-8.00016->

- 9.
- [5] A.B. Spierings, K. Dawson, K. Kern, F. Palm, K. Wegener, SLM-processed Sc- and Zr- modified Al-Mg alloy: Mechanical properties and microstructural effects of heat treatment, *Mater. Sci. Eng. A*. 701 (2017) 264–273. <https://doi.org/10.1016/j.msea.2017.06.089>.
- [6] Q. Jia, P. Rometsch, S. Cao, K. Zhang, X. Wu, Towards a high strength aluminium alloy development methodology for selective laser melting, *Mater. Des.* 174 (2019) 107775. <https://doi.org/10.1016/j.matdes.2019.107775>.
- [7] D. Bayoumy, D. Schliephake, S. Dietrich, X.H. Wu, Y.M. Zhu, A.J. Huang, Intensive processing optimization for achieving strong and ductile Al-Mn-Mg-Sc-Zr alloy produced by selective laser melting, *Mater. Des.* 198 (2021) 109317. <https://doi.org/10.1016/j.matdes.2020.109317>.
- [8] R. Ma, C. Peng, Z. Cai, R. Wang, Z. Zhou, X. Li, X. Cao, Effect of bimodal microstructure on the tensile properties of selective laser melt Al-Mg-Sc-Zr alloy, *J. Alloys Compd.* 815 (2020) 152422. <https://doi.org/10.1016/j.jallcom.2019.152422>.
- [9] Z. Wang, X. Lin, N. Kang, Y. Hu, J. Chen, W. Huang, Strength-ductility synergy of selective laser melted Al-Mg-Sc-Zr alloy with a heterogeneous grain structure, *Addit. Manuf.* 34 (2020) 101260. <https://doi.org/10.1016/j.addma.2020.101260>.
- [10] Q. Jia, P. Rometsch, P. Kürsteiner, Q. Chao, A. Huang, M. Weyland, L. Bourgeois, X. Wu, Selective laser melting of a high strength Al-Mn-Sc alloy: Alloy design and strengthening mechanisms, *Acta Mater.* 171 (2019) 108–118. <https://doi.org/10.1016/j.actamat.2019.04.014>.
- [11] A.B. Spierings, K. Dawson, T. Heeling, P.J. Uggowitzer, R. Schäublin, F. Palm, K. Wegener, Microstructural features of Sc- and Zr-modified Al-Mg alloys processed by selective laser melting, *Mater. Des.* 115 (2017) 52–63. <https://doi.org/10.1016/j.matdes.2016.11.040>.
- [12] Q. Jia, F. Zhang, P. Rometsch, J. Li, J. Mata, M. Weyland, L. Bourgeois, M. Sui, X. Wu, Precipitation kinetics, microstructure evolution and mechanical behavior of a developed Al–Mn–Sc alloy fabricated by selective laser melting, *Acta Mater.* 193 (2020) 239–251. <https://doi.org/10.1016/j.actamat.2020.04.015>.
- [13] A.B. Spierings, K. Dawson, P. Dumitraschkewitz, S. Pogatscher, K. Wegener, Microstructure characterization of SLM-processed Al-Mg-Sc-Zr alloy in the heat treated and HIPed condition, *Addit. Manuf.* 20 (2018) 173–181. <https://doi.org/10.1016/j.addma.2017.12.011>.
- [14] E.A. Jägle, Z. Sheng, L. Wu, L. Lu, J. Risse, A. Weisheit, D. Raabe, Precipitation Reactions in Age-Hardenable Alloys During Laser Additive Manufacturing, *JOM*. 68 (2016) 943–949. <https://doi.org/10.1007/s11837-015-1764-2>.
- [15] A.F. Norman, P.B. Prangnell, R.S. McEwen, The solidification behaviour of dilute aluminium-scandium alloys, *Acta Mater.* 46 (1998) 5715–5732. [https://doi.org/10.1016/S1359-6454\(98\)00257-2](https://doi.org/10.1016/S1359-6454(98)00257-2).
- [16] J. Royset, Scandium In Aluminium Alloys: Physical Metallurgy, Properties And Applications, *Metall. Sci. Technol.* 25 (2007) 11–21.
- [17] Y. Harada, D.C. Dunand, Microstructure of Al₃Sc with ternary rare-earth additions, *Mater. Sci. Eng. A* 329 (2002) 686–695. <https://doi.org/10.1016/j.intermet.2008.09.002>.
- [18] Y. Harada, D.C. Dunand, Thermal expansion of Al₃Sc and Al₃(Sc_{0.75}X_{0.25}), *Scr. Mater.* 48 (2003) 219–222. [https://doi.org/10.1016/S1359-6462\(02\)00428-1](https://doi.org/10.1016/S1359-6462(02)00428-1).
- [19] C.B. Fuller, D.N. Seidman, D.C. Dunand, Mechanical properties of Al(Sc,Zr) alloys at ambient and elevated temperatures, *Acta Mater.* 51 (2003) 4803–4814. [https://doi.org/10.1016/S1359-6454\(03\)00320-3](https://doi.org/10.1016/S1359-6454(03)00320-3).

- [20] Y. Harada, D.C. Dunand, Creep properties of Al₃Sc and Al₃(Sc, X) intermetallics, *Acta Mater.* 48 (2000) 3477–3487. [https://doi.org/10.1016/S1359-6454\(00\)00142-7](https://doi.org/10.1016/S1359-6454(00)00142-7).
- [21] C.B. Fuller, D.N. Seidman, Temporal evolution of the nanostructure of Al(Sc,Zr) alloys: Part II-coarsening of Al₃(Sc_{1-x}Zr_x) precipitates, *Acta Mater.* 53 (2005) 5415–5428. <https://doi.org/10.1016/j.actamat.2005.08.015>.
- [22] J.A. Glerum, C. Kenel, T. Sun, D.C. Dunand, Synthesis of precipitation-strengthened Al-Sc, Al-Zr and Al-Sc-Zr alloys via selective laser melting of elemental powder blends, *Addit. Manuf.* 36 (2020) 101461. <https://doi.org/10.1016/j.addma.2020.101461>.
- [23] W. Lefebvre, F. Danoix, H. Hallem, B. Forbord, A. Bostel, K. Marthinsen, Precipitation kinetic of Al₃(Sc,Zr) dispersoids in aluminium, *J. Alloys Compd.* 470 (2009) 107–110. <https://doi.org/10.1016/j.jallcom.2008.02.043>.
- [24] R.J. Schaefer, L.A. Bendersky, D. Shechtman, W.J. Boettinger, F.S. Biancaniello, ICOSAHEDRAL AND DECAGONAL PHASE FORMATION IN Al-Mn ALLOYS., *Metall. Trans. A, Phys. Metall. Mater. Sci.* 17 A (1986) 2117–2125. <https://doi.org/10.1007/BF02645910>.
- [25] D. Shechtman, I. Blech, D. Gratias, J.W. Cahn, Metallic phase with long-range orientational order and no translational symmetry, *Phys. Rev. Lett.* 53 (1984) 1951–1953. <https://doi.org/10.1103/PhysRevLett.53.1951>.
- [26] D.M. Herlach, F. Gillessen, T. Volkman, M. Wollgarten, K. Urban, Phase selection in undercooled quasicrystal-forming Al-Mn alloy melts, *Phys. Rev. B.* 46 (1992) 5203–5210. <https://doi.org/10.1103/PhysRevB.46.5203>.
- [27] L.F. Mondolfo, Manganese in aluminium alloys, The Centre, 1978.
- [28] A. Bahadur, Intermetallic phases in Al-Mn alloys, *J. Mater. Sci.* 23 (1988) 48–54. <https://doi.org/10.1007/BF01174033>.
- [29] K.L. Kendig, D.B. Miracle, Strengthening mechanisms of an Al-Mg-Sc-Zr alloy, *Acta Mater.* 50 (2002) 4165–4175. [https://doi.org/10.1016/S1359-6454\(02\)00258-6](https://doi.org/10.1016/S1359-6454(02)00258-6).
- [30] D. Bayoumy, K. Kwak, T. Boll, S. Dietrich, D. Schliephake, J. Huang, J. Yi, K. Takashima, X. Wu, Y. Zhu, A. Huang, Origin of non-uniform plasticity in a high-strength Al-Mn-Sc based alloy produced by laser powder bed fusion, *J. Mater. Sci. Technol.* 103 (2022) 121–133. <https://doi.org/10.1016/j.jmst.2021.06.042>.
- [31] D. Schliephake, D. Bayoumy, S. Seils, C. Schulz, A. Kauffmann, X. Wu, A.J. Huang, Mechanical behavior at elevated temperatures of an Al-Mn-Mg-Sc-Zr alloy manufactured by selective laser melting, *Mater. Sci. Eng. A.* 831 (2022) 1–8. <https://doi.org/10.1016/j.msea.2021.142032>.
- [32] D.J. Larson, T.J. Prosa, R.M. Ulfig, B.P. Geiser, T.F. Kelly, *Local Electrode Atom Probe Tomography*, Springer New York, 2013. <https://doi.org/10.1007/978-1-4614-8721-0>.
- [33] O.C. Hellman, J.A. Vandenbroucke, J. Rüsing, D. Isheim, D.N. Seidman, Analysis of three-dimensional atom-probe data by the proximity histogram, *Microsc. Microanal.* 6 (2000) 437–444. <https://doi.org/10.1007/s100050010051>.
- [34] P. Kürnsteiner, P. Bajaj, A. Gupta, M.B. Wilms, A. Weisheit, X. Li, C. Leinenbach, B. Gault, E.A. Jägle, D. Raabe, Control of thermally stable core-shell nano-precipitates in additively manufactured Al-Sc-Zr alloys, *Addit. Manuf.* 32 (2020) 100910. <https://doi.org/10.1016/j.addma.2019.100910>.
- [35] I. Polmear, D. St. John, J.F. Nie, M. Qian, *Light Alloys: Metallurgy of the Light Metals*, fifth ed., Elsevier, Oxford, 2017.
- [36] S. Balanetsky, D. Pavlyuchkov, T. Velikanova, B. Grushko, The Al-rich region of the Al-Fe-Mn alloy system, *J. Alloys Compd.* 619 (2015) 211–220. <https://doi.org/10.1016/j.jallcom.2014.08.232>.

- [37] K. Stan-Głowińska, Ł. Rogal, A. Góral, A. Wierzbicka-Miernik, J. Wojewoda-Budka, N. Schell, L. Lityńska-Dobrzyńska, Formation of a quasicrystalline phase in Al–Mn base alloys cast at intermediate cooling rates, *J. Mater. Sci.* 52 (2017) 7794–7807. <https://doi.org/10.1007/s10853-017-1011-z>.
- [38] R.K. Koju, Y. Mishin, Atomistic study of grain-boundary segregation and grain-boundary diffusion in Al-Mg alloys, *Acta Mater.* 201 (2020) 596–603. <https://doi.org/10.1016/j.actamat.2020.10.029>.
- [39] A. Devaraj, W. Wang, R. Vemuri, L. Kovarik, X. Jiang, M. Bowden, J.R. Trelewicz, S. Mathaudhu, A. Rohatgi, Grain boundary segregation and intermetallic precipitation in coarsening resistant nanocrystalline aluminum alloys, *Acta Mater.* 165 (2019) 698–708. <https://doi.org/10.1016/j.actamat.2018.09.038>.
- [40] M.J. Rahman, H.S. Zurob, J.J. Hoyt, Molecular Dynamics Study of Solute Pinning Effects on Grain Boundary Migration in the Aluminum Magnesium Alloy System, *Metall. Mater. Trans. A Phys. Metall. Mater. Sci.* 47 (2016) 1889–1897. <https://doi.org/10.1007/s11661-016-3322-0>.
- [41] K.B. HYDE, A.F. NORMAN, P.B. PRANGNELL, The Growth Morphology and Nucleation Mechanism of Primary L12 Al3Sc Particles in Al-Sc Alloys, *Mater. Sci. Forum.* 331–337 (2000) 1013–1018.
- [42] K.B. Hyde, A.F. Norman, P.B. Prangnell, The growth morphology and nucleation mechanism of primary L12 Al3Sc particles in Al-Sc alloys, *Mater. Sci. Forum.* 331-337 II (2000) 1013–1018.
- [43] D.A. Porter, K.E. Easterling, *Phase Transformations in Metals and Alloys*, second ed., Chapman & Hall, London, 1992. <https://doi.org/10.1017/CBO9781107415324.004>.
- [44] T. Philippe, M. Gruber, F. Vurpillot, D. Blavette, Clustering and local magnification effects in atom probe tomography: A statistical approach, *Microsc. Microanal.* 16 (2010) 643–648. <https://doi.org/10.1017/S1431927610000449>.
- [45] Y. Wang, H.T. Li, Z. Fan, Oxidation of aluminium alloy melts and inoculation by oxide particles, in: *Trans. Indian Inst. Met.*, 2012. <https://doi.org/10.1007/s12666-012-0194-x>.
- [46] K.B. Hyde, A.F. Norman, P.B. Prangnell, The effect of cooling rate on the morphology of primary Al3Sc intermetallic particles in Al-Sc alloys, *Acta Mater.* 49 (2001) 1327–1337. [https://doi.org/10.1016/S1359-6454\(01\)00050-7](https://doi.org/10.1016/S1359-6454(01)00050-7).
- [47] K. Stiller, L. Viskari, G. Sundell, F. Liu, M. Thuvander, H.O. Andrén, D.J. Larson, T. Prosa, D. Reinhard, Atom probe tomography of oxide scales, in: *Oxid. Met.*, 2013: pp. 227–238. <https://doi.org/10.1007/s11085-012-9330-6>.
- [48] M. Karahka, H.J. Kreuzer, Field evaporation of oxides: A theoretical study, *Ultramicroscopy.* 132 (2013) 54–59. <https://doi.org/10.1016/j.ultramic.2012.10.007>.
- [49] M. Simonelli, C. Tuck, N.T. Aboulkhair, I. Maskery, I. Ashcroft, R.D. Wildman, R. Hague, A Study on the Laser Spatter and the Oxidation Reactions During Selective Laser Melting of 316L Stainless Steel, Al-Si10-Mg, and Ti-6Al-4V, *Metall. Mater. Trans. A Phys. Metall. Mater. Sci.* 46 (2015) 3842–3851. <https://doi.org/10.1007/s11661-015-2882-8>.
- [50] M. Tang, P.C. Pistorius, Oxides, porosity and fatigue performance of AlSi10Mg parts produced by selective laser melting, *Int. J. Fatigue.* 94 (2017) 192–201. <https://doi.org/10.1016/j.ijfatigue.2016.06.002>.